Desalination-of water by vapor-phase transport through hydrophobic nanopores

Citation: Lee, Jongho, and Rohit Karnik. "Desalination of Water by Vapor-phase Transport through Hydrophobic Nanopores." Journal of Applied Physics 108.4 (2010): 044315. ©2010 American Institute of Physics

As Published: http://dx.doi.org/10.1063/1.3419751

Publisher: American Institute of Physics (AIP)

Persistent URL: http://hdl.handle.net/1721.1/78853

Version: Final published version: final published article, as it appeared in a journal, conference proceedings, or other formally published context

AIP | Journal of Applied Physics

Desalination of water by vapor-phase transport through hydrophobic nanopores

Jongho Lee and Rohit Karnik

Citation: J. Appl. Phys. 108, 044315 (2010); doi: 10.1063/1.3419751
View online: http://dx.doi.org/10.1063/1.3419751
View Table of Contents: http://jap.aip.org/resource/1/JAPIAU/v108/i4
Published by the American Institute of Physics.

Desalination of water by vapor-phase transport through hydrophobic nanopores

Jongho Lee and Rohit Karnik[a)]
Department of Mechanical Engineering, Massachusetts Institute of Technology, Cambridge, Massachusetts 02139, USA

(Received 12 August 2009; accepted 7 April 2010; published online 24 August 2010)

We propose a new approach to desalination of water whereby a pressure difference across a vapor-trapping nanopore induces selective transport of water by isothermal evaporation and condensation across the pore. Transport of water through a nanopore with saline water on one side and pure water on the other side under a pressure difference was theoretically analyzed under the rarefied gas assumption using a probabilistic framework that accounts for diffuse scattering from the pore walls as well as reflection from the menisci. The analysis revealed that in addition to salinity, temperature, and pressure difference, the nanopore aspect ratio and the probability of condensation of a water molecule incident on a meniscus from the vapor phase, known as the condensation coefficient, are key determinants of flux. The effect of condensation coefficient on mass flux becomes critical when the aspect ratio is small. However, the mass flux becomes independent of the condensation coefficient as the pore aspect ratio increases, converging to the Knudsen flux for long nanopores. For design of a nanopore membrane that can trap vapor, a minimum aspect ratio is derived for which coalescence of the two interfaces on either side of the nanopore remains energetically unfavorable. Based on this design criterion, the analysis suggests that mass flux in the range of 20–70 g/m^2 s may be feasible if the system is operated at temperatures in the range of 30–50 °C. The proposed approach further decouples transport properties from material properties of the membrane, which opens the possibility of engineering membranes with appropriate materials that may lead to reverse osmosis membranes with improved flux, better selectivity, and high chlorine resistance. © *2010 American Institute of Physics*. [doi:10.1063/1.3419751]

I. INTRODUCTION

The increasing demand and depleting resources of water have worsened the fresh water scarcity problem, and the number of people facing water shortage is expected to quadruple by 2025.[1] The scarcity of fresh water is expected to become more serious in developing countries where many diseases and deaths are attributed to the poor quality of water,[2] and also in Middle East and North African countries that are suffering from lack of renewable fresh water.[2,3] This water shortage problem will require development of effective technologies for desalination of brackish or sea water to meet the demands of agriculture and drinking water. Reverse osmosis (RO) is being increasingly adopted worldwide as an energy efficient technology for water purification.[4] Development of asymmetric membranes[5] and polyamide composite membranes prepared by interfacial polymerization[6,7] have enabled RO to be competitive with thermal processes for large-scale desalination applications. RO is more economical in the aspect of energy cost compared to thermal processes that require more energy due to the latent heat of water.[2] Membrane-based RO has almost reached thermodynamic efficiencies for desalination[8] but RO membranes suffer from some persistent issues including fouling, scaling, and requirement of large membrane areas due to limited flux.[4] Polyamide, the most widely used selective RO membrane material, suffers from low tolerance to chlorine, making the membranes susceptible to biofouling.[9–11] Low rate of boron rejection of RO process is also an issue and conventional RO systems rarely satisfy the boron concentration level that World Health Organization guideline recommends.[12,13] Furthermore, there is a trade-off between membrane area and efficiency due to the limited flux per unit area, and between selectivity and permeability, which is limited by material properties.[14] Further improvements in RO membranes that enable larger flux without compromising selectivity and have increased resistance to fouling are therefore needed.

Advances in nanofluidics promise membranes with improved control over their nanostructure, better selectivity, or decreased viscous losses.[15–19] For example, membranes incorporating carbon nanotubes that allow flow of water with low viscous loss are being developed for desalination of water.[15,20] New nanofluidic transport mechanisms thus have the potential to make a significant impact on energy conversion and clean water technologies through development of better membranes. In the present study, we suggest a new type of RO membrane that uses vapor-phase transport through hydrophobic nanopores for desalination of water. We theoretically explore transport of water through the nanopore using a probabilistic model that incorporates rarefied gas dynamics, ballistic transport, and emission and reflection of water molecules at liquid-vapor interfaces. We study the effect of nanopore geometry, salinity, temperature, applied pressure, and interfacial reflection probability on the trans-

[a)]Author to whom correspondence should be addressed. Electronic mail: karnik@mit.edu.

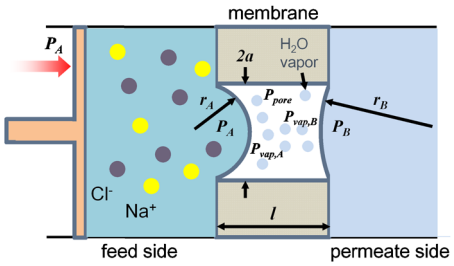

FIG. 1. (Color online) Schematic diagram of a hydrophobic nanopore with liquid-vapor interfaces on either side. Application of pressure greater than the osmotic pressure on the saline water side results in vapor-phase transport of water across the nanopore.

port of water molecules through the nanopore. We further estimate upper bounds on the performance characteristics of RO membranes that incorporate this mechanism.

II. CONCEPT OF RO MEMBRANE INCORPORATING VAPOR-TRAPPING NANOPORES

We propose a membrane that consists of hydrophobic nanopores that trap vapor by virtue of their hydrophobicity and small size, separating the saline feed water on one side and the desalinated permeate water on the other side (Fig. 1). Two water menisci are formed on either sides of the pore and mass transfer occurs only in the form of evaporation at one meniscus, transport of water vapor through the nanopore, and condensation at the other meniscus. The salt concentrations and pressures on either side of the nanopore as well as the temperature determine the equilibrium vapor pressure at each meniscus. If a pressure that exceeds the osmotic pressure is applied on the feed water (saline) side, a vapor pressure difference is generated across the nanopore, resulting in a net flux of water across the pore through evaporation at one interface and condensation at the other interface. Since transport occurs in the vapor phase, the process is selective and only allows water molecules to cross the nanopore. Furthermore, the nanopore is isothermal due to the small length scale and conduction through the nanopore wall material; thus, energy required for evaporation is immediately recovered by condensation.

Transport of water vapor across a vapor-trapping membrane with water on either side has been used for desalination in a technique known as direct contact membrane distillation.[21–23] However, this method relies on a temperature difference to drive transport of water, and is subject to high thermal losses. The present approach replaces the temperature difference by a pressure difference, thereby eliminating thermal losses.

Generally, gas transport in a pore occurs by four different mechanisms: Knudsen diffusion, molecular diffusion, viscous flow, and surface diffusion.[24,25] The large osmotic pressure necessitates small pore diameters less than ~200 nm to prevent wetting. Since the mean free path for water vapor at 20–50 °C is about 1–5 μm, we assume that vapor-phase transport through the pores occurs primarily by Knudsen diffusion. Studies of wetting properties of carbon nanotubes show sharp transitions between nonwetted and wetted states.[16,26] In addition, the water vapor adsorption on

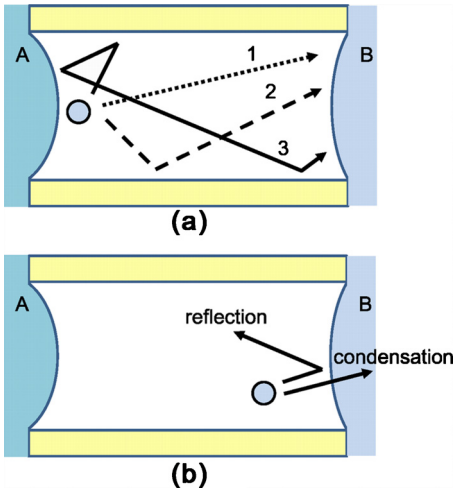

FIG. 2. (Color online) Schematic diagram showing some potential trajectories of molecules inside the nanopore. (a) trajectories the molecule takes from meniscus A to B. (1) meniscus A → meniscus B (ballistic transport), (2) meniscus A → wall → meniscus B, (3) meniscus A → wall → meniscus A → wall → meniscus B. (b) Upon reaching meniscus B, the molecule can either condense or undergo reflection.

pure hydrophobic surfaces such as silicalite-1 and beta zeolites is negligibly small.[27,28] Membrane distillation which incorporates intrinsically hydrophobic porous membranes does not have severe wetting issues from water adsorption in the hydrophobic pores. Furthermore, adsorption of water molecules on hydrophobic surfaces is confined to hydrophilic defects;[29–31] adsorption on such a defect and subsequent emission of a molecule is equivalent to a scattering event from the wall. When hydrophobic and hydrophilic surfaces are patterned in close proximity, it has been shown that water vapor condenses on the hydrophilic patterned sites in preference to the hydrophobic ones.[30] Due to the small length scale of the nanopore, water vapor may be expected to condense on the menisci rather than on the pore surface. In this study, we therefore assume that transport of water through the nanopore by surface flow is negligible as compared to Knudsen diffusion. While Knudsen diffusion theory is known to be valid for the pore diameters down to 2 nm,[32] the classical Knudsen diffusion coefficient is defined only in the limit of an infinite pore length. The predicted Knudsen flux diverges to infinity as the pore length approaches zero; thus, calculation of flux in pores of finite length requires a different approach. Similarly, a model for transport through a hydrophobic pore must also consider the effects of the menisci.

We therefore developed a general model based on a transmission probability framework that accounts for finite nanopore length, rates of evaporation, and condensation, as well as reflection and condensation probabilities at the liquid-vapor interfaces (Fig. 2).

III. PROBABILITY OF TRANSMISSION OF WATER MOLECULES ACROSS A NANOPORE

Let $\varphi_{A,B}$ be defined as the probability that a molecule emitted (by evaporation) from meniscus A condenses at meniscus B. If the rates of evaporation at each meniscus are known, the net flux of water through the nanopore can be

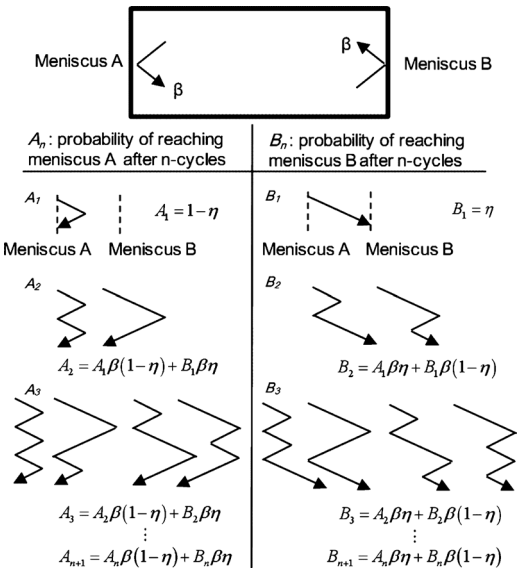

FIG. 3. Possible paths and probabilities of molecules emitted from meniscus A until they condense at either meniscus A or B. In the arrow diagrams, the leftmost position indicates meniscus A, the center position indicates scattering from the pore walls, and the rightmost position indicates meniscus B. For example, in the diagram for A_2, the molecule that leaves meniscus A can arrive at meniscus A (after scattering from the pore walls), be reflected from the meniscus A, and arrive again at A by a similar process (left), or the molecule emitted from A can reach meniscus B, be reflected from meniscus B, and arrive at meniscus A (right).

calculated in terms of $\varphi_{A,B}$ (which equals $\varphi_{B,A}$ by symmetry). $\varphi_{A,B}$ can be further expressed in terms of two distinct probabilities: (a) η, the probability with which a molecule that leaves one meniscus arrives at the other meniscus also known as the transmission probability and (b) σ, the condensation coefficient, which is the probability that a water molecule incident on the liquid-vapor meniscus condenses at the meniscus (Fig. 2).

To calculate $\varphi_{A,B}$, we can consider all possible ways in which a molecule emitted from meniscus A finally condenses at either meniscus A or B (Fig. 3). A molecule which has evaporated from meniscus A is transported to the other meniscus B with transmission probability η. This transmission probability includes the cases where that the molecule arrives at meniscus B after collision(s) with the wall and without any collision with the pore wall. However, this molecule also can return to meniscus A with probability $1-\eta$ after scattering from the wall. We call the transport of a molecule leaving one meniscus and arriving at the other meniscus or back to the same meniscus [after scattering event(s) from pore walls] as one cycle, i.e., after one cycle, the molecule will reach either meniscus A or B. This molecule will then condense with a probability σ on the meniscus it arrived at, or be reflected with a probability $\beta(=1-\sigma)$. If the molecule is reflected from the meniscus A or B, it will start its flight again from the meniscus it was reflected on. We define A_n as the probability that a molecule emitted from meniscus A arrives back at meniscus A after n cycles, and B_n as the probability that a molecule emitted from meniscus A arrives at meniscus B after n cycles. Therefore the probability that a molecule condenses on meniscus A after n cycles is $(1-\beta)A_n$, and that on meniscus B is $(1-\beta)B_n$. A molecule reflected from meniscus A with the probability βA_n will start its $n+1^{\text{th}}$ cycle flight toward meniscus B, and vice versa.

As shown in Fig. 3, if a molecule arrives at meniscus A at the $n+1^{\text{th}}$ cycle, there are two paths that it could have taken after the n^{th} cycle. The first path is that the molecule arrived at meniscus A and was reflected from it, and left meniscus A but was scattered from the wall, and finally reached meniscus A. The probability of this path is $A_n\beta(1-\eta)$. The second path is that the molecule reached meniscus B and was reflected, and transported back to meniscus A. The corresponding probability is $B_n\beta\eta$. Therefore, A_{n+1} can be obtained as

$$A_{n+1} = A_n\beta(1-\eta) + B_n\beta\eta. \tag{1}$$

With similar reasoning, B_{n+1} is also calculated as

$$B_{n+1} = A_n\beta\eta + B_n\beta(1-\eta). \tag{2}$$

Then, the following relation can be obtained:

$$A_n + B_n = \beta(A_{n-1} + B_{n-1}) = \cdots = \beta^{n-1}(A_1 + B_1) = \beta^{n-1}. \tag{3}$$

The probability $\varphi_{A,A}$ and $\varphi_{A,B}$ that a molecule that has evaporated from meniscus A finally condensates on meniscus A and B, respectively, can now be expressed as follows:

$$\varphi_{A,A} = (1-\beta)\sum_{n=1}^{\infty} A_n, \tag{4}$$

$$\varphi_{A,B} = (1-\beta)\sum_{n=1}^{\infty} B_n. \tag{5}$$

Then, it can be readily shown that $\varphi_{A,A}+\varphi_{A,B}=1$. This simply means that molecules evaporated from a meniscus must eventually condense either on meniscus A or B. When we solve for A_n, the following relation is obtained:

$$A_{n+1} = A_n\beta(1-\eta) + B_n\beta\eta = \alpha A_n + \beta^n\eta, \tag{6}$$

where $\alpha=\beta(1-2\eta)$. Therefore, A_n can be expressed as follows:

$$A_n = \alpha^{n-1}A_1 + \alpha^{n-2}\beta\eta + \alpha^{n-3}\beta^2\eta + \cdots + \alpha\beta^{n-2}\eta + \beta^{n-1}\eta = \alpha^{n-1}A_1 + \beta^{n-1}\eta\frac{1-\left(\frac{\alpha}{\beta}\right)^{n-1}}{1-\frac{\alpha}{\beta}}. \tag{7}$$

Then we can calculate $\varphi_{A,A}$ and $\varphi_{A,B}$

$$\varphi_{A,A} = (1-\beta)\sum_{n=1}^{\infty} A_n = 1 - \frac{\eta}{2\eta\beta - \beta + 1}, \tag{8}$$

$$\varphi_{A,B} = 1 - \varphi_{A,A} = \frac{\eta}{2\eta\beta - \beta + 1}. \tag{9}$$

Using the fact that $\beta=1-\sigma$ (by definition), we can write

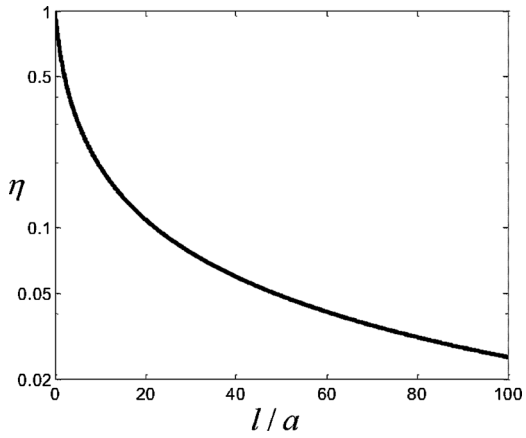

FIG. 4. Probability of transmission of a molecule across a cylindrical nanopore with length l and radius a [(from Berman (Ref. 34)].

$$\varphi_{A,B} = \frac{\eta}{2\eta(1-\sigma)+\sigma}. \tag{10}$$

Alternatively, we can derive Eq. (10) by using a method analogous with that used in heat transfer by radiation (Appendix A). For practically encountered contact angles up to 120°, we can neglect the effect of meniscus curvature on η and assume the pore geometry to be cylindrical (see Appendix B). We further assume that the whole system is isothermal, which is a reasonable approximation even in the case of membrane materials with a relatively poor thermal conductivity (see Appendix C). With these assumptions, we can take advantage of the fact that the transmission probability in Eq. (10) is equivalent to the transmission probability across a pore of finite length. Transmission probability was first introduced by Clausing[33] to obtain pressure-driven flux of a rarefied gas through a pore of finite length. Here, we use the transmission probability η as calculated by Berman[34] for a pore of finite length under the diffuse scattering assumption (Fig. 4). η is a function only of the pore aspect ratio l/a with a maximum value of 1 occurring at zero pore length, corresponding to ballistic transport. η decreases with increasing l/a and converges to $8/3(l/a)$ for long pores, which is consistent with Knudsen diffusion.

The value of σ is difficult to predict and must be obtained empirically. Although a number of experiments have been carried out to evaluate σ for water, the literature indicates a large spread in its value ranging from 0.01 to 1.[35] Eames *et al.*[36] reviewed the literature and concluded that the condensation coefficient for water was likely to be between 0.5 and 1. Relatively earlier literature[37–39] evaluated the evaporation coefficient in the range 0.01–0.05 while more recent literature[40–42] suggested values greater than 0.5. Bonacci[43] attributed the very low value of σ to the difficulties of accurate measurement of surface temperature. Following these arguments, the condensation (or evaporation) coefficient σ is assumed to range from 0.5 to 1.0 in the present study. In addition, it is also assumed that σ is independent of curvature of meniscus and salt concentration.

IV. RELATION BETWEEN MASS FLUX AND DRIVING PRESSURE

The rate of evaporation is related to the vapor pressure and probability of condensation σ. The rate of absorption of water molecules at the liquid-vapor interface is equal to the product of the rate of incidence and the probability of condensation, which, at equilibrium, must equal the rate of evaporation. For temperatures up to 50 °C, the density of water vapor deviates from that predicted by kinetic theory of gases by less than 0.4%; we therefore use the kinetic gas theory to estimate the rate of incidence. This is known as the Hertz hypothesis,[36,44] which gives the rate of gross evaporation per unit area at each meniscus as

$$\dot{m}_{e,A(B)} = \sigma\sqrt{\frac{M}{2\pi RT_s}}P_{\mathrm{vap},A(B)}. \tag{11}$$

Here, T_s is the temperature of the interface, $P_{\mathrm{vap},A(B)}$ is the equilibrium vapor pressure of water at meniscus A (or B) at temperature T_s, R is the universal gas constant, and M is the molecular weight of water. Using Kelvin's equation[45] and Raoult's law, the equilibrium vapor pressures at each meniscus can be expressed in terms of the pressure drop across the menisci as follows

$$P_{\mathrm{vap},A} = P^0_{\mathrm{vap}}\exp\left(\frac{\Delta P_A V_m}{RT_s}\right)x_w \simeq P^0_{\mathrm{vap}}\left(1+\frac{\Delta P_A V_m}{RT_s}\right)x_w, \tag{12}$$

$$P_{\mathrm{vap},B} = P^0_{\mathrm{vap}}\exp\left(\frac{\Delta P_B V_m}{RT_s}\right) \simeq P^0_{\mathrm{vap}}\left(1+\frac{\Delta P_B V_m}{RT_s}\right). \tag{13}$$

$\Delta P_{A(B)}$ is the pressure difference across the meniscus ($\Delta P_A = P_A - P_{\mathrm{pore}}$; $\Delta P_B = P_B - P_{\mathrm{pore}}$), P^0_{vap} is the vapor pressure of water at temperature T_s, V_m is the molar volume of liquid water, and x_w is the mole fraction of the feed water. For applied pressures less than 100 bar, P_{pore} deviates only slightly from the equilibrium vapor pressure P^0_{vap}, since $\Delta P_{A(B)} V_m \ll RT_s$. Raoult's law is valid here since the activity coefficient of water in NaCl solution is unity (=1.000) for salt concentrations below 1 M.[46] At equilibrium, the pressure difference across the nanopore $\Delta P = \Delta P_A - \Delta P_B$ is equal to the osmotic pressure. Increasing the pressure difference across the nanopore beyond the osmotic pressure results in $P_{\mathrm{vap},A} > P_{\mathrm{vap},B}$ and net transport of water across the nanopore. The vapor pressure difference across the pore is a driving force to mass transport and given as

$$P_{\mathrm{vap},A} - P_{\mathrm{vap},B} = P^0_{\mathrm{vap}}\left[\left(1+\frac{\Delta P_A V_m}{RT_s}\right)(x_w - 1) + \frac{\Delta P_A V_m}{RT_s} - \frac{\Delta P_B V_m}{RT_s}\right]. \tag{14}$$

The osmotic pressure $\Delta\pi$ for the NaCl concentration considered here (<1 M) can be obtained as

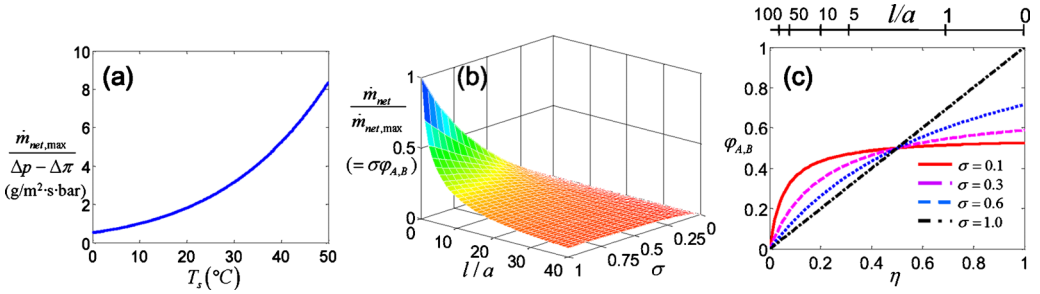

FIG. 5. (Color online) (a) Specific ratio of theoretical maximum mass flux to driving pressure at different temperatures. (b) Net mass flux normalized by theoretical maximum mass flux through a nanopore. The theoretical maximum mass flux indicates the mass flux for $\sigma=1$ and $l/a=0$ ($\eta=1$). (c) Variation in $\varphi_{A,B}$ with η and σ. The scale bar on the top of (c) represents the pore aspect ratio l/a corresponding to η.

$$\Delta\pi = -\frac{RT_s}{V_m}\ln x_w \simeq \frac{RT_s}{V_m}(1-x_w). \tag{15}$$

Therefore, the above equation can be approximated as follows:

$$P_{\mathrm{vap},A} - P_{\mathrm{vap},B} = P^0_{\mathrm{vap}}\left[\frac{(\Delta P-\Delta\pi)V_m}{RT_s} - \frac{\Delta P_A V_m}{RT_s}\frac{\Delta\pi V_m}{RT_s}\right]. \tag{16}$$

Since the second term in the parenthesis is much smaller than the first one, we finally obtain the following relation:

$$P_{\mathrm{vap},A} - P_{\mathrm{vap},B} = \frac{(\Delta P-\Delta\pi)V_m}{RT_s}P^0_{\mathrm{vap}}. \tag{17}$$

Knowing the rate of evaporation [Eqs. (13)–(15)] and the probability $\varphi_{A,B}$ that a water molecule emitted by evaporation condenses on the other meniscus [Eq. (10)], the net mass flux per unit area across the nanopore is given by

$$\dot{m}_{\mathrm{net}} = \varphi_{A,B}\dot{m}_{e,A} - \varphi_{B,A}\dot{m}_{e,B} = \varphi_{A,B}(\dot{m}_{e,A} - \dot{m}_{e,B})$$
$$= \frac{\sigma\eta}{2\eta(1-\sigma)+\sigma}\sqrt{\frac{M}{2\pi RT_s}}\left(\frac{\Delta P-\Delta\pi}{RT_s}V_m\right)P^0_{\mathrm{vap}}(T_s), \tag{18}$$

where ΔP is the total pressure drop across the nanopore.

Seawater (or brackish water) is characterized in terms of total dissolved solids (TDS) ranging from 15 000 to 50 000 ppm (corresponding to 0.26 M to 0.90 M NaCl), with the TDS of standard seawater being 35 200 ppm (0.62 M NaCl solution). TDS for brackish water ranges from 1500 to 15 000 (0.026 M to 0.26 M NaCl solution). The corresponding osmotic pressure is about 13 to 44 bar for seawater and 1.3 to 13 bar for brackish water, although seawater with the same TDS as that of NaCl solution has a lower osmotic pressure due to presence of higher mass solutes.[4] RO plants for desalination of sea water typically operate at pressures ranging from around 55–80 bar.[4]

V. CHARACTERISTICS OF VAPOR-PHASE TRANSPORT THROUGH A NANOPORE

The theoretical maximum mass flux occurs when there is no resistance to transport across the nanopore, i.e., $\eta=\sigma=1$. Under these conditions, the rate of condensation is equal to the rate of incidence of water molecules at the meniscus, and the rate of evaporation is also maximized [see Eq. (11)]. Molecules that evaporate at one meniscus undergo ballistic transport to the other meniscus, where they condense. The maximum flux per unit driving pressure ($\Delta P-\Delta\pi$) depends on the interface temperature and vapor pressure of water, and can be expressed as:

$$\frac{\dot{m}_{\mathrm{net,max}}}{\Delta P-\Delta\pi} = \sqrt{\frac{M}{2\pi RT_s}}\frac{V_m}{RT_s}P^0_{\mathrm{vap}}(T_s). \tag{19}$$

This maximum mass flux increases rapidly with temperature, closely following the increase in vapor pressure with temperature [Fig. 5(a)]. As the vapor pressure increases with temperature, the modulation of the equilibrium vapor pressure due to application of external pressure across the nanopore also increases; in fact, Eqs. (12) and (13) show that the modulation is directly proportional to P^0_{vap}, the vapor pressure of water.

The ratio of the mass flux to the theoretical maximum mass flux equals $\sigma\varphi_{A,B}$, which is determined by the pore aspect ratio l/a (directly related to η) and the condensation coefficient σ. Figure 5(b) shows that $\varphi_{A,B}$ equals the transmission probability η when $\sigma=1$. This case corresponds to zero resistance to mass flux at the menisci so that all water molecules incident on the meniscus undergo condensation. $\eta=1$ corresponds to the case of a very short nanopore with ballistic transport, where $\varphi_{A,B}$ approaches $1/(2-\sigma)$. In this case, $\varphi_{A,B}$ equals 1/2 for very small σ; each molecule undergoes several reflections at the menisci, with equal chance of condensation at either meniscus. Thus, when $\eta>0.5$ (corresponding to $l/a<0.57$), a smaller probability of condensation decreases $\varphi_{A,B}$. When $\eta<0.5$ (corresponding to $l/a>0.57$), a smaller probability of condensation actually increases $\varphi_{A,B}$ [Fig. 5(c)]. While it may seem counterintuitive, it is easily seen that a molecule emitted from one meniscus has a high probability of returning to the original meniscus several times before reaching the other meniscus if the pore is long (small η). A small value of σ increases the probability of reflection from the original meniscus, thereby increasing the chance of reaching the other meniscus after undergoing multiple reflections at the original meniscus. Interestingly, $\eta=0.5$ corresponds to a pore aspect ratio (l/a) of 0.57, in which case σ has no effect on $\varphi_{A,B}$.

Figure 6 illustrates the effect of temperature, pore geometry, and condensation coefficient on the net mass flux per unit driving pressure. Figures 6(a) and 6(b) reveal that the

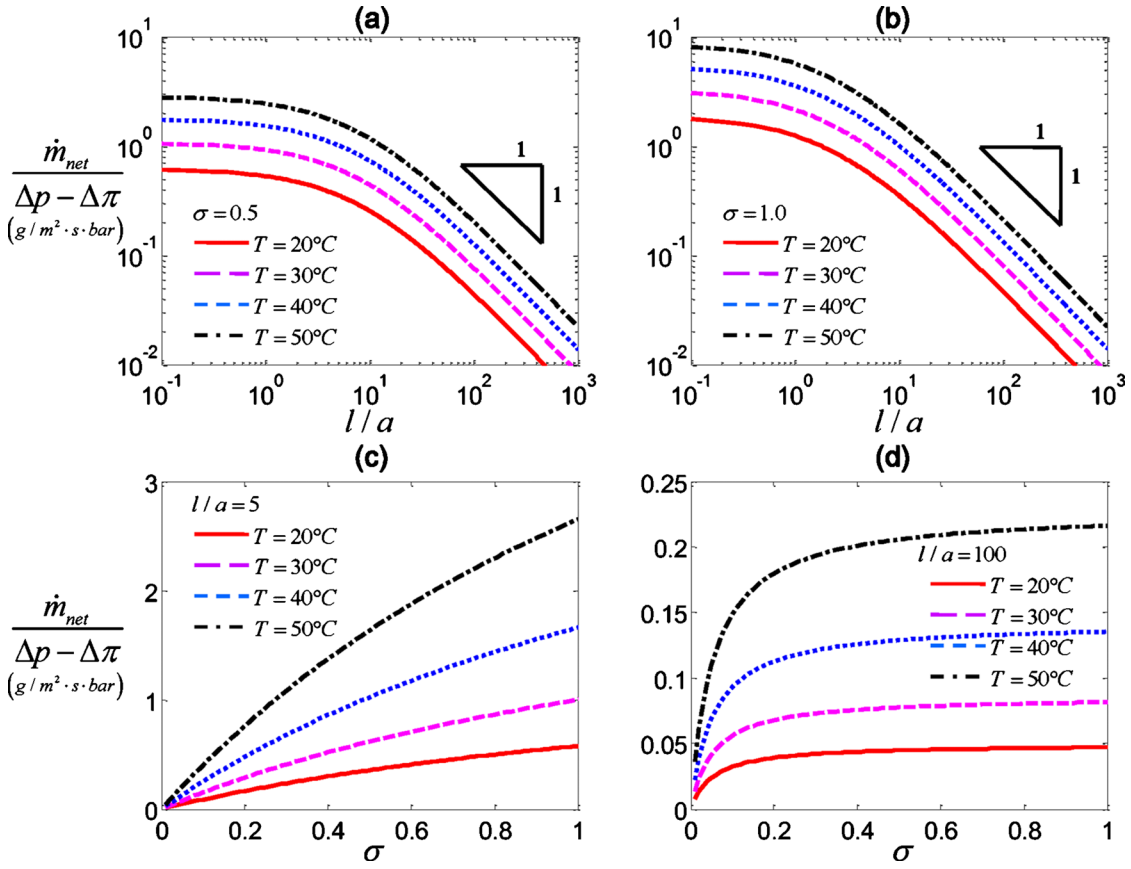

FIG. 6. (Color online) Effect of pore aspect ratio l/a and condensation coefficient σ on the mass flux through the pore per unit driving pressure at different temperatures. (a) $\sigma=0.5$; (b) $\sigma=1.0$; (c) $l/a=5$; and (d) $l/a=100$.

mass flux monotonically decreases as the pore length is increased. For very short nanopores ($\eta \to 1$), the flux is about threefold higher at $\sigma=1$ as compared with $\sigma=0.5$; since a higher σ directly increases not only the rate of evaporation [see Eq. (11)] but also $\varphi_{A,B}$ by reducing mass transport resistance at menisci. In the case of sufficiently long pores, the net flux decreases inversely as l/a, which is consistent with Knudsen flux with a constant Knudsen diffusion coefficient. In all cases, it is seen that the flux increases with increasing temperature due to the increasing vapor pressure. Figures 6(c) and 6(d) show the effect of the condensation coefficient σ on the mass flux with T_s and l/a as parameters. For small pore length, for instance $l/a=5$ (where $\eta=0.23$) as shown in Fig. 6(c), the mass flux increases with σ. At very small values of σ, the linear variation is due to the linear increase in the rate of evaporation as given by Eq. (11); $\varphi_{A,B}$ remains close to 0.5 since σ is small, as shown by Eq. (10). On the other hand, for long pores [$l/a=100$ shown in Fig. 6(d)], the mass flux rapidly increases with σ and then becomes independent of σ. For very small values of σ, the mass flux is directly proportional to σ, since a low value of σ brings $\varphi_{A,B}$ close to 0.5. Above a moderate value of σ, resistance due to reflection at the menisci becomes negligible and transport is governed only by the transmission probability η. A close examination of Eq. (10) shows that $\varphi_{A,B}$ is inversely proportional to σ for small values of η, and this effect is exactly offset by the increase in rate of evaporation with σ [Eq. (11)]. Thus, the mass flux becomes nearly independent of σ and for very long pores and converges to its value corresponding to $\sigma=1$. Since η approaches $8/3(l/a)$ for long pores, the mass flux converges to

$$\dot{m}_{\text{net}} = \frac{8}{3(l/a)}\sqrt{\frac{M}{2\pi RT_s}}(P_{\text{vap},A} - P_{\text{vap},B})$$

$$= \frac{2}{3}\bar{\alpha}aM\frac{P_{\text{vap},A} - P_{\text{vap},B}}{lRT_s} \quad (l/a \gg 1). \tag{20}$$

This expression is the same as that derived for Knudsen diffusion flux through a pore with pressures $P_{\text{vap},A}$ and $P_{\text{vap},B}$ at either end. It implies that for sufficiently long pores, the actual vapor pressure at the each meniscus is maintained close to the equilibrium vapor pressure according to the local condition of the meniscus, which is often assumed to be the boundary condition to analyze mass flux in membrane distillation.[23] From Eq. (10), the condition for this assumption to be valid is seen to be $2\eta \ll \sigma$.

VI. CRITERIA FOR WETTING OF A HYDROPHOBIC NANOPORE

Implementation of the proposed technique for desalination will require appropriate choice of membranes with hydrophobic nanopores. The ability of the nanopores to resist wetting under a large applied pressure is critical for the operation of such a membrane. Several studies have examined the wetting and dewetting behavior of water in hydrophobic

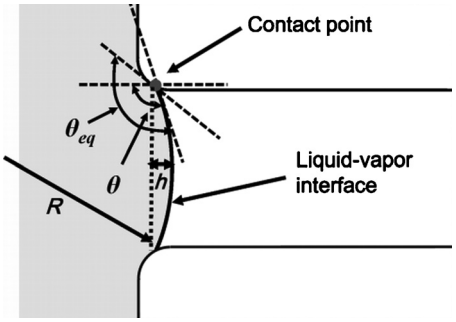

FIG. 7. Detailed configuration of liquid-vapor interface at the feed side. θ_{eq} denotes equilibrium contact angle satisfying Young–Laplace equation ($\gamma_{sl} - \gamma_{sv} + \gamma_{lv} \cos \theta_{eq} = 0$) and θ denotes the angle between a line tangential to interface and pore axis, which satisfies mechanical force equilibrium.

mesopores.[47–49] Using the Young–Laplace equation, the criterion that a pore of radius a resists wetting is

$$a \leq \left| \frac{2\gamma_{lv} \cos \theta_{eq}}{\Delta P_A} \right|, \tag{21}$$

where γ_{lv} is surface tension of the water and vapor interface, θ_{eq} is the equilibrium contact angle, and ΔP_A is the pressure difference across the interface. This criterion has been found to be valid for pores as small as 2.6 nm in diameter.[47] For a contact angle of $\theta_{eq}=120°$ and a pressure difference $\Delta P_A = 50$ bar, the critical pore diameter is 28 nm.

For a given pore radius, the aspect ratio l/a needs to be minimized to achieve a high mass flux. However, even if the pore radius satisfies Eq. (21), there is a critical aspect ratio below which wetting of the pore becomes energetically favorable,[49] which may lead to merging of the two interfaces depending on the actual kinetic barrier. This condition depends on the length of the nanopore and can be expressed in terms of the pore aspect ratio. For a given radius of pore and pressure difference that can sustain a meniscus the interface will settle at a certain contact point with an equilibrium contact angle where force equilibrium is also satisfied. The angle θ between tangential line of the interface and pore axis at the contact point is determined by mechanical equilibrium, and is generally different from equilibrium contact angle θ_{eq} (see Fig. 7). If the interface at the feed side moves in to fill the pore, PV work will be expended in forming new liquid-solid surface and a part of the work will be compensated by merging of the two liquid interfaces

$$-\int_{V_0}^{0} \Delta P_A dV + \Delta E = (\gamma_{sl} - \gamma_{sv}) A_w - \gamma_{lv}(A_f + A_p), \tag{22}$$

where γ_{sl} and γ_{sv} are interfacial energies of solid-liquid and solid-vapor interfaces, respectively. V_0, A_w, A_f, and A_p denote the initial pore volume occupied by vapor and air, the areas of pore wall, menisci at feed, and permeate sides, respectively. ΔE is the additional energy to induce the filling and therefore the filling would not occur spontaneously when $\Delta E > 0$. The PV work by applied pressure $P_{applied}$ moving interface then becomes

$$W_{PV} = -\int_{V_0}^{0} (P_{applied} - P_{pore}) dV = \Delta P_A V_0, \tag{23}$$

where P_{pore} remains constant to keep saturation condition. Assuming spherical shape of meniscus, the above equation becomes

$$\Delta P_A V_0 + \Delta E = 2(\gamma_{sl} - \gamma_{sv}) \pi a l - \gamma_{lv}(2\pi R h + \pi a^2), \tag{24}$$

where V_0, ΔP_A, R, and h are given as

$$V_0 = \pi a^2 l + \pi \left(\frac{a}{\cos \theta} \right)^3 \left[\frac{2}{3} - \frac{2}{3} \sin \theta - \frac{1}{3} \cos^2 \theta \sin \theta \right], \tag{25}$$

$$\Delta P_A = -\frac{2\gamma_{lv}}{a} \cos \theta, \tag{26}$$

$$\frac{R}{a} = -\frac{1}{\cos \theta}, \tag{27}$$

$$\frac{h}{a} = \frac{R}{a} - \left[\left(\frac{R}{a} \right)^2 - 1 \right]^{1/2}. \tag{28}$$

Simplifying these equations, the criterion that satisfies $\Delta E > 0$ becomes

$$\frac{l}{a} > \frac{1}{\cos \theta - \cos \theta_{eq}} \left[\frac{1}{2} + \frac{1}{1 + \sin \theta} \right], \tag{29}$$

where $\cos \theta = -a\Delta P_A / 2\gamma_{lv}$ and $\cos \theta_{eq} = -a_{max} \Delta P_A / 2\gamma_{lv}$. For a given finite pore length, this criterion always gives a critical pore radius that is smaller than that calculated from the Young–Laplace criterion [Eq. (21)]. The wetting and dewetting behavior is not well-characterized for short hydrophobic pores bounded by menisci on either side. Thus, while it is possible that the Young–Laplace criterion is sufficient to prevent wetting, the thermodynamic criterion given by Eq. (29) is more conservative of the two. For example, for a contact angle of $\theta_{eq}=120°$, pressure difference $\Delta P_A = 50$ bar with NaCl of 0.62 M, and a pore radius of 5 nm, the minimum pore length that makes wetting energetically unfavorable is 15.2 nm. The minimum pore length at 20 °C for different pore radii is given in Fig. 8. Since the surface tension does not change significantly in the temperature range of 20–50 °C (Table I), the minimum pore length is not significantly affected by temperature.

VII. MASS FLUX THROUGH A MEMBRANE INCORPORATING VAPOR-TRAPPING NANOPORES

For a given pore radius that is smaller than the critical pore radius according to the Young–Laplace criterion, Eq. (29) predicts a minimum pore length for wetting to be thermodynamically unfavorable. Using this conservative pore length, Fig. 9 depicts the mass flux [Eq. (18)] through a membrane consisting of cylindrical pores with 40% porosity for different pore radii and driving pressures for a 0.62 M NaCl feedwater solution and a contact angle of 120°. For a given pressure drop, as the pore radius increases, the minimum aspect ratio $(l/a)_{min}$ also increases, so that, the trans-

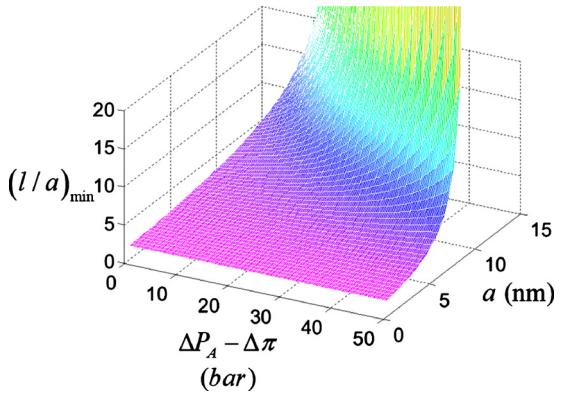

FIG. 8. (Color online) Minimum pore length that makes pore wetting energetically unfavorable at different values of the applied pressure and pore radius. Contact angle of 120°, NaCl concentration of 0.62 M, and temperature of 20 °C are assumed.

mission probability and mass flux are decreased. It is seen that nanopores with diameters in the 5–10 nm range might be practical for implementing this approach of desalination. Similarly, the flux increases significantly if temperature is increased from 20–50 °C, and moderately as σ increases from 0.5 to 1. The red region with zero flux indicates that the pore radius is too large to sustain the applied pressure without wetting the pores. Thus, the highest flux occurs for the smaller pores. In practice, the validity of Eq. (29) will have to be tested experimentally; it is entirely possible that shorter aspect ratios and therefore higher fluxes can be obtained even when wetting is thermodynamically favorable.

The predicted flux through the membrane is in the range of or larger than typical experimentally observed flux through current RO membranes.[50–52] Although we have not considered system-level issues such as concentration polarization and design of the membrane module, these results suggest that the proposed technique may be promising for desalination of water. For example, Fig. 9 indicates that the maximum flux that can be achieved for a 40% porous membrane at 50 bar driving pressure is approximately 18 g/m^2 s at 20 °C and 70 g/m^2 s at 50 °C. RO membrane literature reports flux in the range of 5–22 g/m^2 s for composite polyamide membranes.[50–53] Several different polymers and treatments have been explored for improving the selectivity,[6,54] flux,[55] resistance to chlorine,[56] and boron rejection;[12] however, there is a trade-off between these parameters and improvement of one aspect tends to adversely affect the other aspects. Commercial membranes typically yield fluxes based on nominal membrane area in the range of 7.7–10.6 g/m^2 s for driving pressures of 27 bar.[51] The theoretical results presented here suggest that membranes based

TABLE I. Values of parameters used in the study [R: universal gas constant (=8.31 J/mol·K), M: molar weight of water (=1.80×10^{-2} kg/mol), and V_m: molar volume of liquid water (=1.80×10^{-5} m^3/mol)].

Temperature (T_s) (°C)	Surface tension (γ_{lv}) (N/m)	Vapor pressure (P^0_{vap}) (Pa)
20	7.28×10^{-2}	2.31×10^3
30	7.12×10^{-2}	4.20×10^3
40	6.96×10^{-2}	7.30×10^3
50	6.79×10^{-2}	1.22×10^4

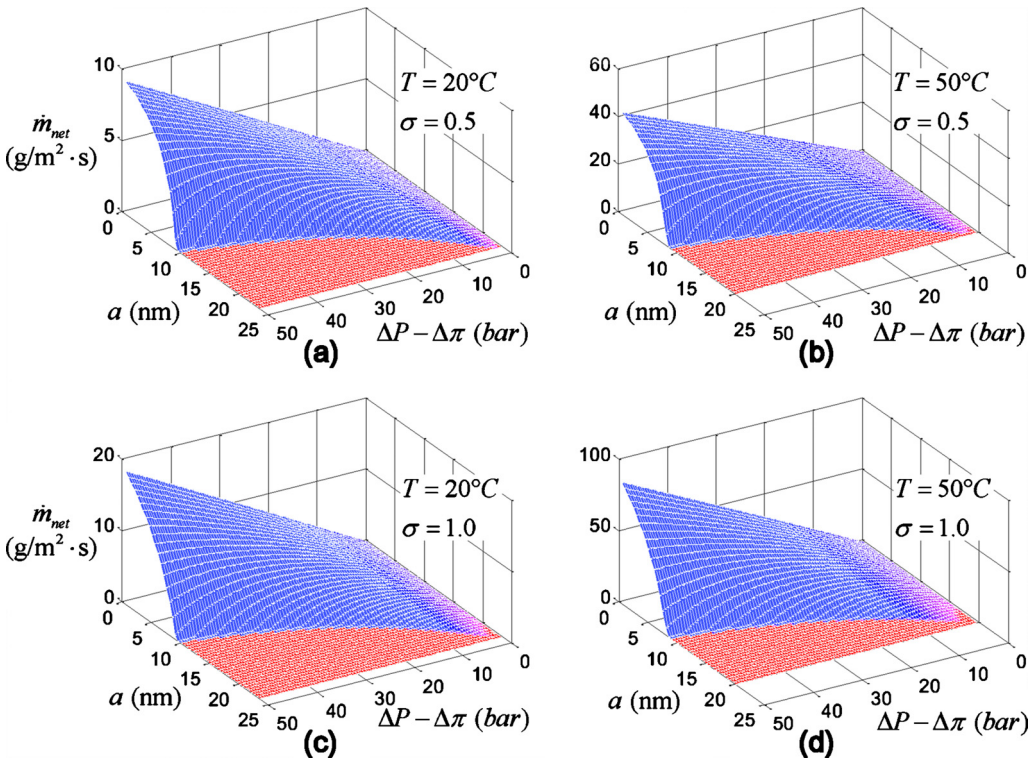

FIG. 9. (Color online) Predicted mass flux through membrane for different pore sizes and driving pressures at the minimum pore aspect ratio l/a which makes wetting thermodynamically unfavorable. Contact angle of 120°, NaCl concentration of 0.62 M, and 40% membrane porosity are assumed. (a) T=20 °C, σ=0.5; (b) T=50 °C, σ=0.5; (c) T=20 °C, σ=1.0; and (d) T=50 °C, σ=1.0.

on hydrophobic nanopores are promising for improving the flux as compared to current RO membranes, especially if they are operated at temperatures that are modestly above room temperature. Moreover, the currently used RO membranes do not have adequate chemical resistance to chlorine,[4,56] which is widely used as an industrial disinfectant to control biofouling. The inherent coupling between the permeability, selectivity, chlorine resistance, and boron rejection that confounds optimization of polymeric membranes is decoupled in the case of the present approach. It is then conceivable that chlorine-resistant hydrophobic materials can be found for the manufacture of the proposed nanoporous membranes for desalination of water. With advances in nanotechnology, several options including self-assembly[57–59] and nanofabrication[19,60] are available to fabricate the proposed membranes. For example, such membranes may be fabricated by modifying a small length near the entrance of nanopores in alumina membranes[61,62] with a hydrophobic coating. We recently realized such a membrane with short hydrophobic pores by evaporation of gold on alumina pores followed by modification using an alkanethiol self-assembled monolayer. The detailed fabrication procedure and the following flux measurements will be the subject of a future publication.

VIII. CONCLUSION

In conclusion, we have proposed a new technique for desalination of water using pressure-driven transport through hydrophobic membranes. Pore diameters in the range of 10 nm are adequate to sustain the applied pressure for desalination of seawater. Theoretical analysis of transport through these membranes shows that the pore aspect ratio and the probability of condensation of water molecules incident on a meniscus are the key factors that determine the flux. The flux is largely governed by condensation coefficient for short pore while the flux becomes independent of the condensation coefficient and corresponds to Knudsen flux as the aspect ratio becomes larger. The nanopore aspect ratio over which merging of two interfaces is energetically unfavorable is utilized as a design condition for nanopore membrane. Based on this criterion and moderately elevated temperature, the analysis suggests that the proposed method has the potential to provide high flux membranes with the added advantage of decoupling the material properties from the transport properties, which may allow for the development of chlorine-resistant and high boron rejection membranes. Further development of this technique may lead to improved membranes for desalination by RO.

ACKNOWLEDGMENTS

The authors would like to thank the King Fahd University of Petroleum and Minerals in Dhahran, Saudi Arabia, for funding the research reported in this paper through the Center for Clean Water and Clean Energy at MIT and KFUPM.

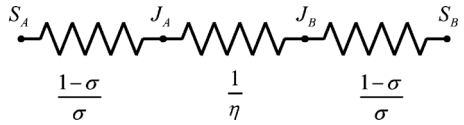

FIG. 10. Configuration of mass transport resistances from analogy with radiation heat transfer.

APPENDIX A: HEAT TRANSFER ANALOGY FOR CALCULATION OF TRANSPORT THROUGH THE NANOPORE

An alternative way to obtain the net mass flux is by using an analogy from radiation heat transfer.[63] As shown in Fig. 10, the mass transport system can be modeled as three resistances in series due to reflection from the two menisci and scattering from the pore wall. Let $S_{A(B)}$ be the maximum gross evaporation rate through meniscus A(B). The actual rate of gross evaporation is $\sigma S_{A(B)}$. In addition, define $G_{A(B)}$ as mass flux incident on meniscus A(B), and $J_{A(B)}$ as mass flux leaving meniscus A(B) by emission and reflection. Then the mass flux $\dot{m}_{\text{net}}$ leaving meniscus A is given as:

$$\dot{m}_{\text{net}} = J_A - G_A = \sigma S_A - \sigma G_A, \tag{A1}$$

where $J_{A(B)} = \sigma S_{A(B)} + (1-\sigma) G_{A(B)}$ from the above definition. For meniscus B, the above equation is applicable in the same way except that the sign of $\dot{m}_{\text{net}}$ reverses. $\dot{m}_{\text{net}}$ can be obtained as follows:

$$\dot{m}_{\text{net}} = \frac{\sigma}{1-\sigma}(S_A - J_A). \tag{A2}$$

Therefore, the mass transfer resistance through the meniscus between $S_{A(B)}$ and $J_{A(B)}$ is $(1-\sigma)/\sigma$. In terms of incoming fluxes J_A and J_B at each meniscus, the net mass flux through the pore using transmission probability η is given as

$$\dot{m}_{\text{net}} = \eta(J_A - J_B). \tag{A3}$$

Therefore, the resistance from the pore wall can be simply $1/\eta$. Then the total resistance of this system is given as

$$R_{\text{total}} = \frac{2(1-\sigma)}{\sigma} + \frac{1}{\eta}. \tag{A4}$$

With the fluxes of mass source S_A and S_B, the net mass flux is obtained as

$$\dot{m}_{\text{net}} = \frac{S_A - S_B}{R_{\text{total}}} = \sqrt{\frac{M}{2\pi R T_s}}(P_{\text{vap},A} - P_{\text{vap},B}) \Big/ \left(\frac{2(1-\sigma)}{\sigma} + \frac{1}{\eta} \right) = \sigma \varphi_{A,B} \sqrt{\frac{M}{2\pi R T_s}}(P_{\text{vap},A} - P_{\text{vap},B}), \tag{A5}$$

where $S_{A(B)} = \sqrt{M/2\pi R T_s} P_{\text{vap},A(B)}$.

APPENDIX B: EFFECT OF MENISCUS CURVATURE ON THE TRANSMISSION PROBABILITY

The net mass flux may be affected by the meniscus curvature because the larger surface can emit a larger number of molecules and the scattering between the meniscus and the pore wall may be different compared with a flat meniscus. Clausing[33] obtained integral equation for transmission probability η of pore connecting two reservoirs with different

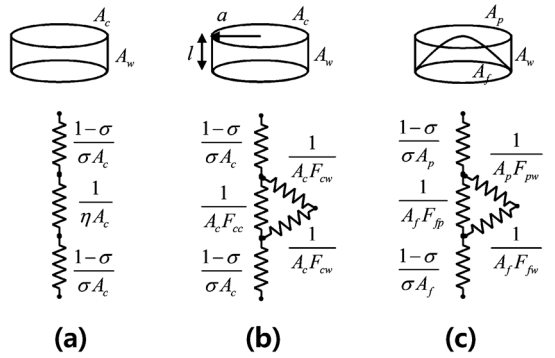

FIG. 11. Resistance networks for estimating the effect of meniscus curvature on transmission probability using the radiation heat transfer analogy. A_c, A_w, A_f, and A_p denote the area of cross section of pore, pore wall, menisci at feed, and permeate sides, respectively. F_{cc} and F_{cc} and F_{cw} indicate view factors between the two menisci, and from a meniscus to the pore wall, respectively, for flat interfaces. F_{fp}, F_{fw}, and F_{pw} denote view factors from the meniscus on the feed side to that on the permeate side, from the meniscus on the feed side to the pore wall, and from the meniscus on the permeate side to the pore wall, respectively, assuming that the meniscus on the feed side is curved (maximum possible curvature at a contact angle of 120°) and that on the permeate side is flat.

pressures. Therefore η includes the effect of variation in incidental rate and directions of molecules on the pore wall. When we use heat radiation analogy to calculate the mass flux, we employ view factors F's to obtain mass transport resistance across the pore instead of using η. However, this approach assumes a certain mean pressure (it is analogous to assuming that an insulating surface is at a uniform temperature) along the entire length of the pore. This assumption is valid for short pores, but fails for longer pores. The heat transfer analogy can account for meniscus curvature using view factors, and we therefore compare the difference in transmission probability introduced by the curvature using the heat transfer analogy. Figure 11 shows three different mass transport resistance networks for small l/a corresponding to pores with flat and curved menisci. The first case corresponds to flat menisci and the exact transmission resistance obtained from η. The second case corresponds to flat menisci and transmission resistance obtained using view factors from the heat transfer analogy. The third case corresponds to a curved meniscus on one side and transport resistances obtained using the heat transfer analogy.

Assuming contact angle of 120°, the aspect ratio at which meniscus at feed side touches the other side is $l/a=0.27$. At this pore length, the difference of mass flux between the case employing η [Fig. 11(a)] and that using view factors [Fig. 11(b)] is less than 0.1%. The mass flux for curved meniscus configuration by using view factors [Fig. 11(c)] is about 3% larger than the former two cases for σ ranging from 0 to 1. The curved surface modestly increases the mass flux due to the increased emission surface area, but it is offset by the altered view factors. This tendency is similar when $l/a=0.81$, where the mass flux is slightly increased ($\sim$3.5%) compared to the case using η with flat meniscus assumed.

When l/a becomes larger, for example, $l/a>3$, the difference between the mass fluxes obtained by employing η and view factors for flat surfaces becomes larger. However, the mass fluxes for the curved and flat surfaces by using view factors are still within 3%. Therefore it would be reasonable to conclude that the effect of the curved surface on mass flux is negligible to within 5%.

APPENDIX C: TEMPERATURE DIFFERENCE ACROSS A MEMBRANE INCORPORATING VAPOR-TRAPPING NANOPORES

The membrane material and porosity are important considerations for minimizing the temperature difference across the membrane. Membrane porosity is defined as the void fraction of the whole membrane volume. Since the membrane considered here is assumed to have straight cylindrical pores, the porosity is the same as the ratio of total cross section area of pores to membrane surface area. Typically, commercial membrane porosity ranges from 20% to 60%. The mass flux through the pore will increase with porosity, but the temperature difference between feed and permeate sides will become larger due to the latent heat transfer by evaporation and condensation. Then the vapor pressure at feed side will, therefore, decrease and it will reduce the vapor transport. Conduction through the nonporous part on the membrane is needed for maintaining nearly isothermal conditions. When the heat transfer by evaporation and condensation is balanced by heat conduction through the membrane, we have

$$\Delta T = \frac{\dot{m} h_{fg} l}{k(1 - A_{\text{pore}}/A_{\text{total}})}, \tag{C1}$$

where A_{total} and A_{pore} are total membrane area and total area occupied by pores, respectively. $\dot{m}$ is the mass flux per unit total area, which can be obtained from Eq. (18) and membrane porosity. h_{fg} is latent heat of vaporization of water, k is the thermal conductivity of the membrane material, ΔT is temperature difference across the membrane, and l denotes membrane thickness or the length of the pores. For example, the vapor pressure difference at 20 °C across the membrane by applying 50 bar on the feed side is 35 Pa. Based on polytetrafluoroethylene membrane of thermal conductivity[64] of 0.27 W/m K as one possible material with 40% porosity, $\sigma=1.0$, $a=5$ nm, and $l=20$ nm (note that $(l/a)_{\min}=3.1$), the mass flux is 5.4 g/m^2 s when the salt concentration is 0.62 M NaCl. The temperature difference obtained by balancing heat conduction and latent heat transport is 0.0016 °C. This temperature difference reduces the vapor pressure difference by 0.7%. As another example, with a temperature of 50 °C and the same pore radius, the vapor pressure difference induced by the latent heat transport decreases by 2.9% at $l=20$ nm, 3.9% at $l=50$ nm, 4.4% at $l=100$ nm, and by 5.4% at $l=5$ μm. Figure 12 shows the decrease in vapor pressure difference for temperature of 50 °C and the same σ, salt concentration, and porosity as pore radius and length vary with an aspect ratio larger than $(l/a)_{\min}$. For a given pore length, the decrease is smaller with smaller pore radius due to lower flux. Therefore membranes with smaller pore size and length are more preferable. The maximum variation does not exceed 12.5% based on a thermal conductivity of 0.27 W/m K, and is correspondingly lower for membrane materials with higher thermal conductivities. In the present

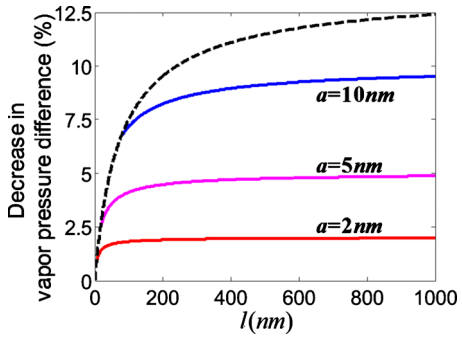

FIG. 12. (Color online) Decrease in vapor pressure difference across a membrane with thermal conductivity of 0.27 W/m K. Applied pressure of 50 bar, temperature of 50 °C, NaCl concentration of 0.62 M, condensation probability of 1.0, and porosity of 40% are assumed. Dashed line indicates the vapor pressure difference variation at minimum aspect ratio $(l/a)_{\min}$.

study, we therefore neglect the temperature gradient effect and assume isothermal transport.

[1]R. Engelman, R. P. Cincotta, B. Dye, T. Gardner-Outlaw, and J. Wisnewski, *People in the Balance: Population and Natural Resources at the Turn of the Millennium* (Population Action International, Washington, D.C., 2000).
[2]J. E. Miller, *Review of water resources and desalination technologies* (Sandia National Laboratories Report, SAND2003-0800, 2003), WWW document (http://www.sandia.gov/water/docs/MillerSAND2003_0800.pdf).
[3]R. P. Cincotta, R. Engelman, and D. Anastasion, *The Security Demographic: Population and Civil Conflict After the Cold War* (Population Action International, Washington, D.C., 2003).
[4]C. Fritzmann, J. Lowenberg, T. Wintgens, and T. Melin, Desalination **216**, 1 (2007).
[5]S. Loeb and S. Sourirajan, U.S. Patent No. 3133132 (May 1964).
[6]J. Cadotte, U.S. Patent No. 4277344 (July 1981).
[7]B. H. Jeong, E. M. V. Hoek, Y. S. Yan, A. Subramani, X. F. Huang, G. Hurwitz, A. K. Ghosh, and A. Jawor, J. Membr. Sci. **294**, 1 (2007).
[8]M. A. Shannon, P. W. Bohn, M. Elimelech, J. G. Georgiadis, B. J. Marinas, and A. M. Mayes, Nature (London) **452**, 301 (2008).
[9]J. Glater, S. K. Hong, and M. Elimelech, Desalination **95**, 325 (1994).
[10]P. T. Cardew and M. S. Le, *Membrane Processes* (Royal Society of Chemistry, Cambridge, 1999).
[11]M. Soltanieh and W. N. Gill, Chem. Eng. Commun. **12**, 279 (1981).
[12]Y. Magara, A. Tabata, M. Kohki, M. Kawasaki, and M. Hirose, Desalination **118**, 25 (1998).
[13]M. Taniguchi, M. Kurihara, and S. Kimura, J. Membr. Sci. **183**, 259 (2001).
[14]A. Prakash Rao, S. V. Joshi, J. J. Trivedi, C. V. Devmurari, and V. J. Shah, J. Membr. Sci. **211**, 13 (2003).
[15]J. K. Holt, H. G. Park, Y. M. Wang, M. Stadermann, A. B. Artyukhin, C. P. Grigoropoulos, A. Noy, and O. Bakajin, Science **312**, 1034 (2006).
[16]G. Hummer, J. C. Rasaiah, and J. P. Noworyta, Nature (London) **414**, 188 (2001).
[17]C. Wang, M. Waje, X. Wang, J. M. Tang, R. C. Haddon, and Y. S. Yan, Nano Lett. **4**, 345 (2004).
[18]Z. L. Liu, X. H. Lin, J. Y. Lee, W. Zhang, M. Han, and L. M. Gan, Langmuir **18**, 4054 (2002).
[19]C. C. Striemer, T. R. Gaborski, J. L. McGrath, and P. M. Fauchet, Nature (London) **445**, 749 (2007).
[20]F. Fornasiero, H. G. Park, J. K. Holt, M. Stadermann, C. P. Grigoropoulos, A. Noy, and O. Bakajin, Proc. Natl. Acad. Sci. U.S.A. **105**, 17250 (2008).
[21]S. Srisurichan, R. Jiraratananon, and A. G. Fane, J. Membr. Sci. **277**, 186 (2006).
[22]K. W. Lawson and D. R. Lloyd, J. Membr. Sci. **120**, 123 (1996).
[23]K. W. Lawson and D. R. Lloyd, J. Membr. Sci. **124**, 1 (1997).
[24]E. A. Mason and A. P. Malinauskas, *Gas Transport in Porous Media: The Dusty-Gas Model* (Elsevier, Amsterdam, 1983).
[25]R. E. Cunningham and R. J. J. Williams, *Diffusion in Gases and Porous Media* (Plenum, New York, 1980).
[26]O. Beckstein and M. S. P. Sansom, Proc. Natl. Acad. Sci. U.S.A. **100**, 7063 (2003).
[27]A. Giaya and R. W. Thompson, J. Chem. Phys. **117**, 3464 (2002).
[28]J. Stelzer, M. Paulus, M. Hunger, and J. Weitkamp, Microporous Mesoporous Mater. **22**, 1 (1998).
[29]C. E. Ramachandran, S. Chempath, L. J. Broadbelt, and R. Q. Snurr, Microporous Mesoporous Mater. **90**, 293 (2006).
[30]K. K. Varanasi, M. Hsu, N. Bhate, W. S. Yang, and T. Deng, Appl. Phys. Lett. **95**, 094101 (2009).
[31]F. Cailliez, G. Stirnemann, A. Boutin, I. Demachy, and A. H. Fuchs, J. Phys. Chem. C **112**, 10435 (2008).
[32]B. A. McCool, N. Hill, J. DiCarlo, and W. J. DeSisto, J. Membr. Sci. **218**, 55 (2003).
[33]P. Clausing, J. Vac. Sci. Technol. **8**, 636 (1971).
[34]A. S. Berman, J. Appl. Phys. **36**, 3356 (1965).
[35]R. Marek and J. Straub, Int. J. Heat Mass Transfer **44**, 39 (2001).
[36]I. W. Eames, N. J. Marr, and H. Sabir, Int. J. Heat Mass Transfer **40**, 2963 (1997).
[37]G. Wyllie, Proc. R. Soc. London, Ser. A **197**, 383 (1949).
[38]T. Alty and C. A. MacKay, Proc. R. Soc. London, Ser. A **149**, 104 (1935).
[39]T. Alty, Proc. R. Soc. London, Ser. A **131**, 554 (1931).
[40]A. F. Mills and R. A. Seban, Int. J. Heat Mass Transfer **10**, 1815 (1967).
[41]J. R. Maa, Ind. Eng. Chem. Fundam. **6**, 504 (1967).
[42]K. Nabavian and L. A. Bromley, Chem. Eng. Sci. **18**, 651 (1963).
[43]J. C. Bonacci, A. L. Myers, G. Nongbri, and L. C. Eagleton, Chem. Eng. Sci. **31**, 609 (1976).
[44]S. I. Anisimov, D. O. Dunikov, V. V. Zhakhovskii, and S. P. Malyshenko, J. Chem. Phys. **110**, 8722 (1999).
[45]S. J. Gregg and K. S. W. Sing, *Adsorption, Surface Area, and Porosity* (Academic, London, 1967).
[46]S. I. Sandler, *Chemical, Biochemical, and Engineering Thermodynamics*, 4th ed. (Wiley, New York, 2006).
[47]B. Lefevre, A. Saugey, J. L. Barrat, L. Bocquet, E. Charlaix, P. F. Gobin, and G. Vigier, J. Chem. Phys. **120**, 4927 (2004).
[48]I. Vlassiouk, C. D. Park, S. A. Vail, D. Gust, and S. Smirnov, Nano Lett. **6**, 1013 (2006).
[49]K. Lum and A. Luzar, Phys. Rev. E **56**, R6283 (1997).
[50]P. H. Wolf and S. Siverns, Proceedings of the International Conference on Desalination Costing, Limassol, 2004, pp. 55–62.
[51]M. Wilf and L. Awerbuch, *The Guidebook to Membrane Desalination Technology: Reverse Osmosis, Nanofiltration and Hybrid Systems: Process, Design, Applications and Economics* (Balaban Desalination, L'Aquila, Italy, 2007).
[52]W. E. Mickols, M. Busch, Y. Maeda, and J. Tonner, International Desalination Association World Congress, Singapore, 2005.
[53]M. Taniguchi and S. Kimura, AIChE J. **46**, 1967 (2000).
[54]R. J. Petersen, J. Membr. Sci. **83**, 81 (1993).
[55]A. Kulkarni, D. Mukherjee, and W. N. Gill, J. Membr. Sci. **114**, 39 (1996).
[56]H. I. Kim and S. S. Kim, J. Membr. Sci. **190**, 21 (2001).
[57]M. Khayet, D. E. Suk, R. M. Narbaitz, J. P. Santerre, and T. Matsuura, J. Appl. Polym. Sci. **89**, 2902 (2003).
[58]W. A. Phillip, J. Rzayev, M. A. Hillmyer, and E. L. Cussler, J. Membr. Sci. **286**, 144 (2006).
[59]A. Yamaguchi, F. Uejo, T. Yoda, T. Uchida, Y. Tanamura, T. Yamashita, and N. Teramae, Nature Mater. **3**, 337 (2004).
[60]G. Y. Liu, S. Xu, and Y. L. Qian, Acc. Chem. Res. **33**, 457 (2000).
[61]Z. H. Yuan, H. Huang, and S. S. Fan, Adv. Mater. (Weinheim, Ger.) **14**, 303 (2002).
[62]H. Klauk, U. Zschieschang, J. Pflaum, and M. Halik, Nature (London) **445**, 745 (2007).
[63]A. F. Mills, *Heat Transfer*, 2nd ed. (Prentice-Hall, Upper Saddle River, N.J., 1998).
[64]C. Hall, *Polymer Materials: An Introduction for Technologists and Scientists* (Halsted, New York, 1981).